Supporting Information

Periodic Trends in Olefin Epoxidation over Group IV and V Framework Substituted Zeolite Catalysts: A Kinetic and Spectroscopic Study

Daniel T. Bregante[1] and David W. Flaherty[1,*]

[1]Department of Chemical and Biomolecular Engineering
University of Illinois Urbana-Champaign, Urbana, IL 61801

*Corresponding Author

Phone: (217) 244-2816

Email: dwflhrty@illinois.edu

S1.0 Additional Catalyst Characterization and Verification of Measuring True Kinetics

S1.1 Catalyst Characterization

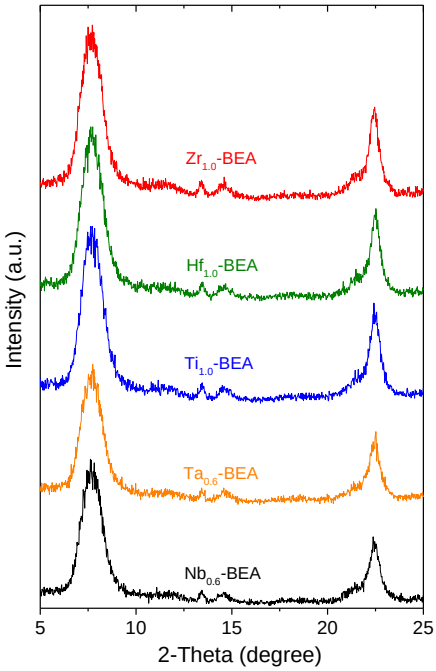

Figure S1. X-ray diffractograms for $Ti_{1.0}$- (blue), $Zr_{1.0}$- (red), $Hf_{1.0}$- (green), $Nb_{0.6}$- (black) and $Ta_{0.6}$-β (orange) taken on a Siemens/Bruker D5000 X-ray diffractometer with Cu Kα radiation (0.15418 nm) at ambient conditions. $Nb_{0.6}$-β data is adapted from ref [6].

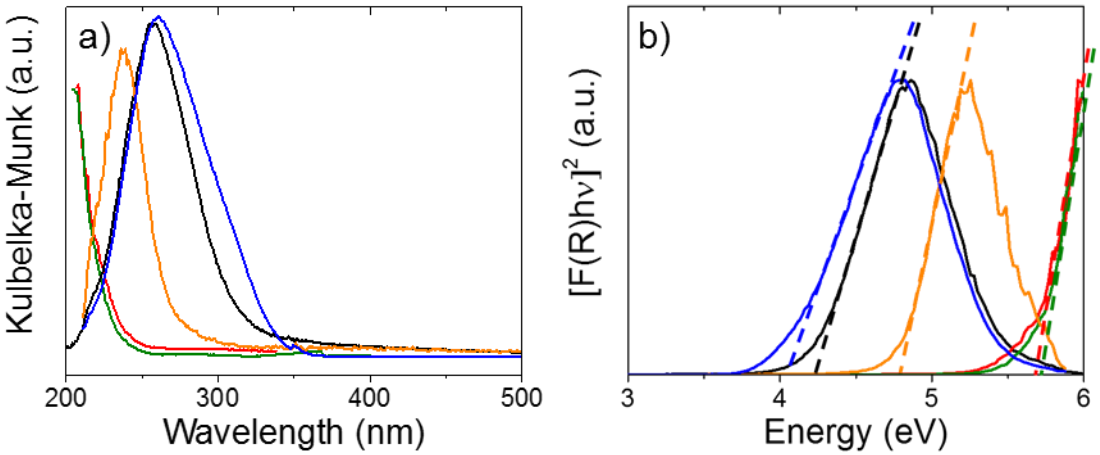

Figure S2. a) UV-vis spectra and b) Normalized tauc plots for $Ti_{0.6}$- (blue), $Nb_{1.0}$- (black) and $Ta_{1.0}$-β (orange), $Zr_{0.6}$- (red), $Hf_{0.6}$- (green). X-axis intercept of dashed lines represents the band edge for each material. $Nb_{0.6}$-β data is adapted from ref [6].

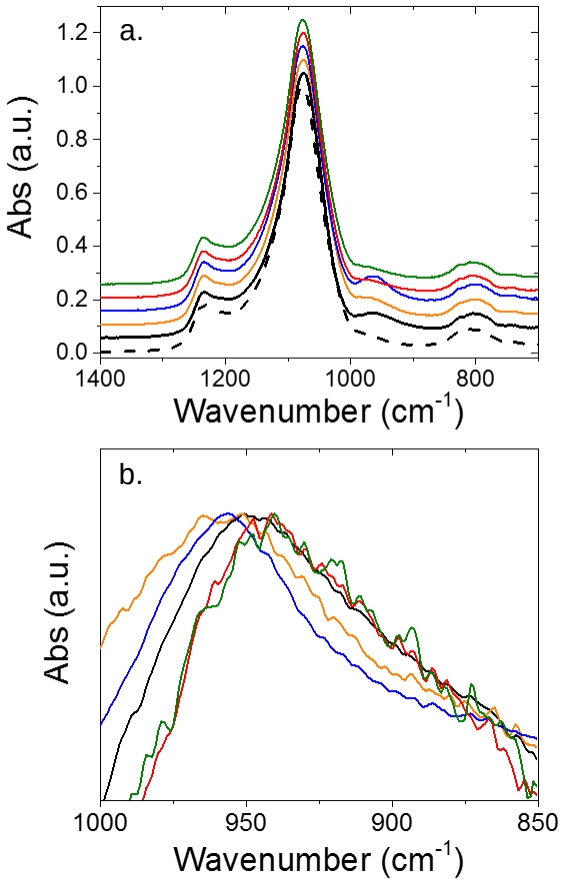

Figure S3. IR spectra for (a) $Ti_{1.0}$- (blue), $Zr_{1.0}$- (red), $Hf_{1.0}$- (green), $Nb_{0.6}$- (black) and $Ta_{0.6}$-β (orange), and Si-β (dashed) obtained at ambient conditions and (b) M-β with Si-β spectra subtracted with normalization to the ~960 cm^{-1} feature to observe ν(Si-O-M) feature. $Nb_{0.6}$-β data is adapted from ref [6].

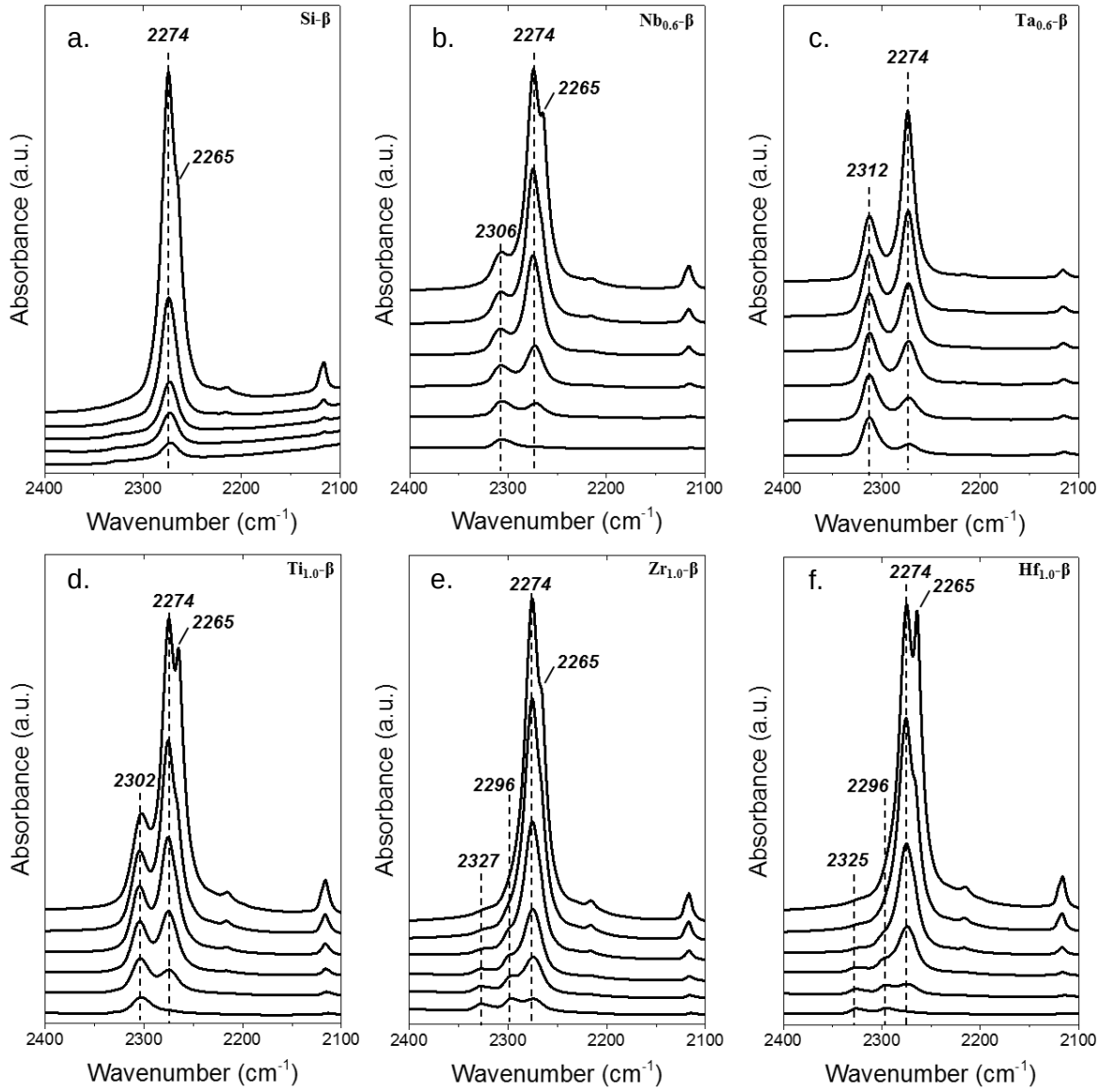

Figure S4. IR spectra of adsorbed CD_3CN (1.0 kPa, 50 cm^3 min^{-1} in He) at 298 K followed by desorption (50 cm^3 min^{-1} He) as the temperature was increased to 423 K (5 K min^{-1}) to resolve Lewis-acid bound ν(C≡N) on (a) Si-β, (b) $Nb_{0.6}$-β, (c) $Ta_{0.6}$-β, (d) $Ti_{1.0}$-β, (e) $Zr_{1.0}$-β, and (f) $Hf_{1.0}$-β. $Nb_{0.6}$-β data is adapted from ref [6].

Figure S4. shows FTIR spectra of CD_3CN adsorbed onto all M-β catalysts, where absorption features between 2260 – 2340 cm^{-1} correspond to the ν(C≡N) mode.[1,2] The absorbance peak located at 2274 cm^{-1} is assigned to CD_3CN hydrogen bonded to surface SiOH groups, while the shoulder at 2265 cm^{-1} is attributed to physisorbed CD_3CN.[1,2] After the surfaces are saturated with CD_3CN (i.e., ν(C≡N) of SiOH-bound CD_3CN stopped increasing), the flow of CD_3CN is stopped and the temperature of the FTIR cell is increased under a constant flow of He (50 cm^3 min^{-1}).

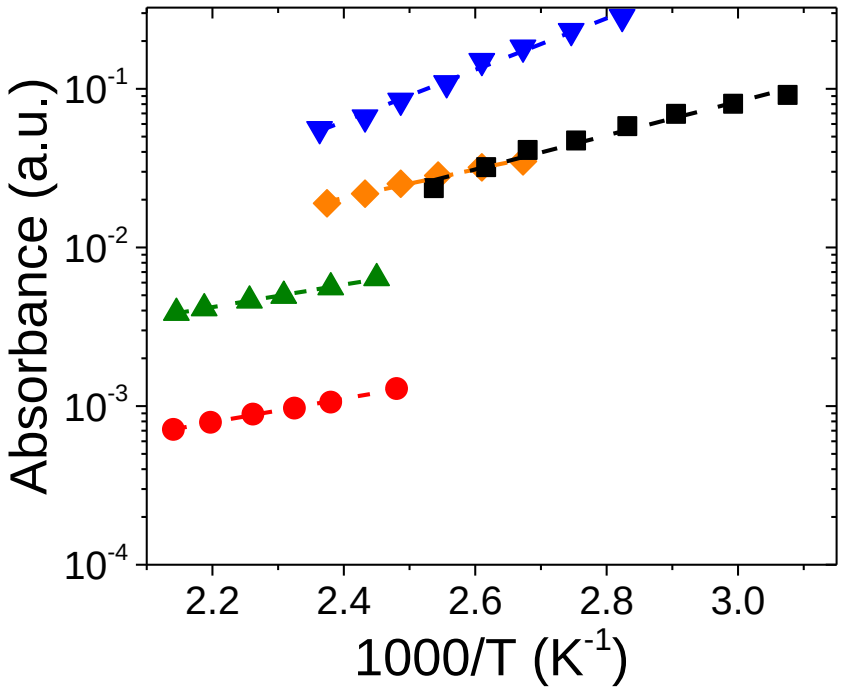

Figure S5. IR absorbances for the Lewis-acid bound ν(C≡N) depicted in Fig. S5b-f. on $Nb_{0.6}$-β (■, 2306 cm^{-1}, Fig. S5b), $Ta_{0.6}$-β (♦, 2312 cm^{-1}, Fig. S5c), $Ti_{1.0}$-β (▼, 2302 cm^{-1}, Fig. S5d), $Zr_{1.0}$-β (●, 2296 cm^{-1}, Fig. S5e), and $Hf_{1.0}$-β (▲, 2296 cm^{-1}, Fig. S5f) as a function of inverse temperature (1.5 kPa CD_3CN, 99 kPa He, 50 cm^3 min^{-1} He) after background subtraction. Dashed lines represent linear fits, whose slope are proportional to the value of ΔH_{CD3CN}. $Nb_{0.6}$-β data is adapted from ref [6].

S1.2 Control Experiments to Test Importance of Mass Transfer

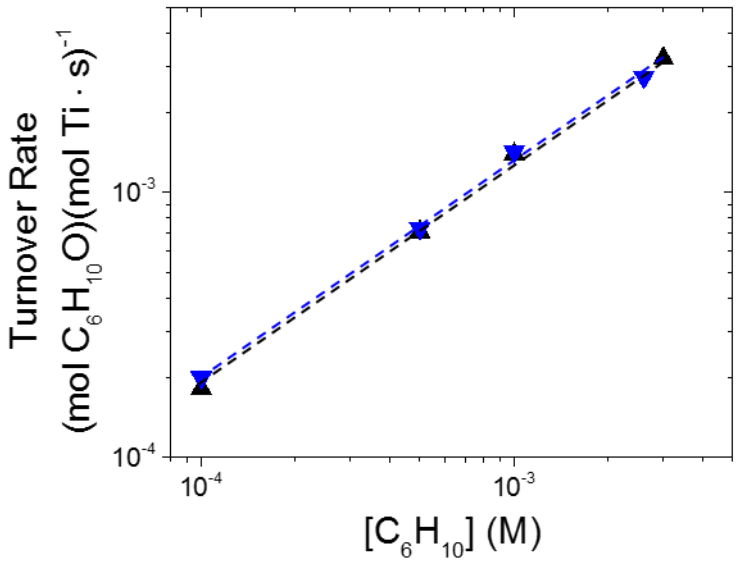

Figure S6. Turnover rates for the formation of C_6H_{10} measured as a function of $[C_6H_{10}]$ on $Ti_{1.0}$-β (▼, 0.01 M H_2O_2, 313 K) and $Ti_{0.1}$-β (▲, 0.01 M H_2O_2, 313 K). Dashed lines are intended to guide the eye.

Figure S6 shows rates for the formation of cyclohexene oxide measured as a function of cyclohexene concentration for multiple metal loadings of Ti in Ti-β. The rate of $C_6H_{10}O$ formation is independent of metal loading (over 0.141 – 1.2 wt. % Ti), which indicates that the Madon-Boudart criterion is satisfied for Ti-β.[5] Under the conditions tested, we see that the turnover rate for $C_6H_{10}O$ formation is proportional to $[C_6H_{10}]$ and independent of $[H_2O_2]$, which corresponds to a simplified rate expression (Section 3.2 of main text) of:

$$\frac{r_E}{[L]} = k_3[C_6H_{10}] \tag{S1}$$

where r_E is the rate of $C_6H_{10}O$ formation, [L] is the total number of metal atoms in the reactor, k_3 is the rate constant for step 3 of scheme 2, and $[C_6H_{10}]$ is the concentration of C_6H_{10}. For a first-order reaction (such as in equation S1), an effective Thiele modulus for a spherical pellet[5] can be defined as:

$$\phi = \left(\frac{k_3 R^2 [C_6H_{10}]}{D_e} \right)^{1/2} \tag{S2}$$

where ϕ is the Thiele modulous, R is the radius of the spherical pellet, $[C_6H_{10}]$ is the bulk concentration of C_6H_{10}, and D_e is the effective diffusivity of C_6H_{10} through the pellet. The Madon-Boudart criterion is an experimental way to determine the relative value of the Thiele modulous, where the independent of turnover rates on metal loading signifies a relatively small Thiele modulous. When the Thiele modulous is small, the rates of diffusion are much greater than those for the inherent kinetics of the reaction (at reactant concentrations equal to that in the

bulk fluid phase), which shows that the measured reaction rates are not corrupted by diffusion restrictions within the catalyt particles.

In Fig. 4 (main text), epoxidation turnover rates decrease in the following order: Ti > Nb > Ta >> Zr ~ Hf under conditions that result in a M-(O_2) saturated surface. Therefore, for all M-β other than Ti, the value of k_3 is much smaller while all other terms are identical. Therefore, the change in k_3 gives a smaller value of the Thiele moduli for Nb-, Ta-, Zr-, and Hf-β than for Ti-β. Therefore, satisfaction of the Madon-Boudart criterion for Ti-β proves that the other M-β are also not mass-transfer limited and all measured reaction rates are reflect only chemical kinetics.

S2. *In Situ* UV-Visible Spectroscopy and Identification of Active Intermediates

S2.1 Sample Raw UV-Vis Spectrum and Method for Processing Spectra

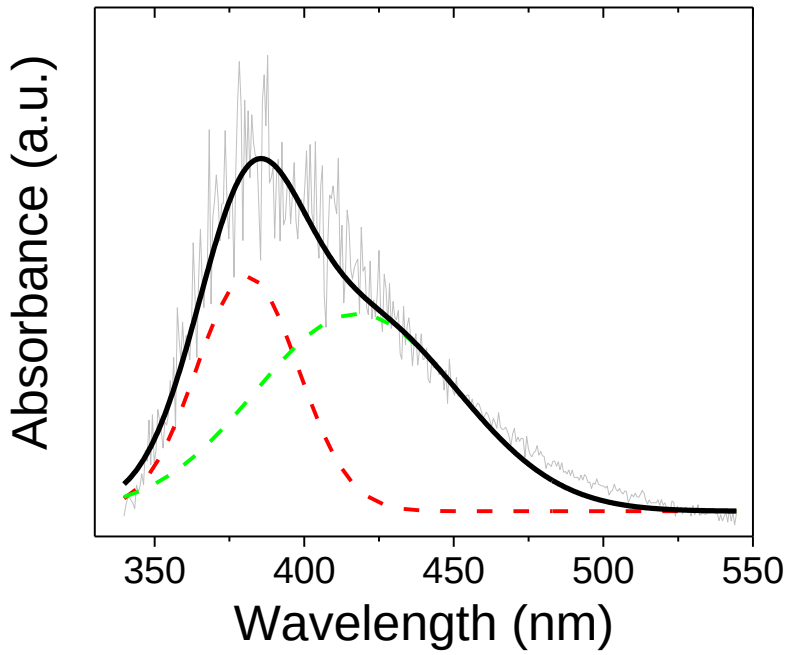

Figure S7. UV-vis absorbance spectrum (raw data, gray) of H_2O_2-treated $Ti_{1.0}$-β at 313 K in flowing CH_3CN (0.4 M H_2O) and smoothed data (bold black line) using a finite fourier transform. Dashed red and green curves represent Gaussian peak fittings, performed in OriginPro®.

S2.2 *In Situ* UV-Vis Spectra with Peak Fits for All M-β Samples

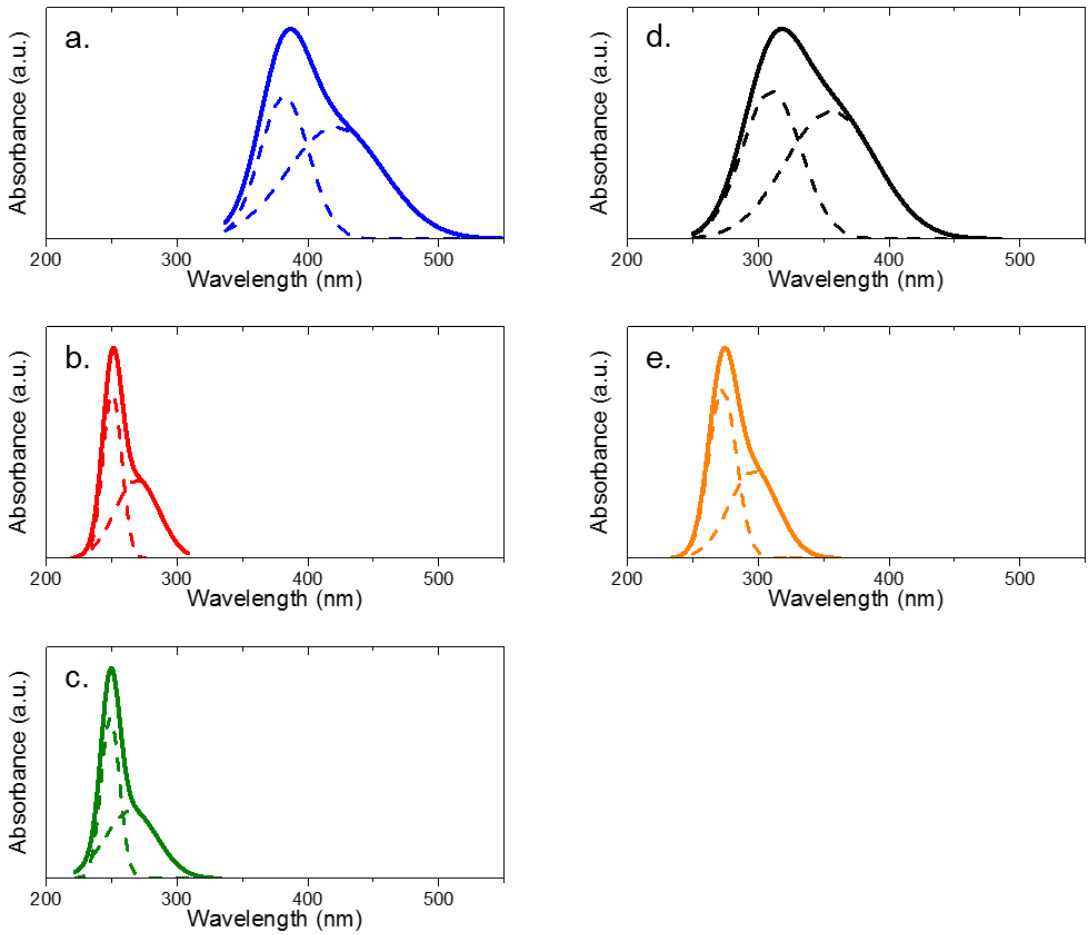

Figure S8. Normalized UV-vis absorbance spectrum of H_2O_2-activated (section 2.4) (a) $Ti_{1.0}$-β, (b) $Zr_{1.0}$-β, (c) $Hf_{1.0}$-β, (d) $Nb_{0.2}$-β, and (e) $Ta_{0.6}$-β in flowing CH_3CN (0.4 M H_2O, 1 cm^3 min^{-1}) at 313 K. Dashed curves represent Gaussian peak fittings (performed in OriginPro®) to show M-$(O_2)^-$ (lower wavelength) and M-OOH/M-$(O_2)^{2-}$ (higher wavelength) species. $Nb_{0.6}$-β data is adapted from ref [6].

Table S1. Ligand to metal charge transfer energies (hν) for the M-OOH/-$(O_2)^{2-}$ and M-$(O_2)^-$ intermediates as detected via *in situ* UV-vis spectra (Fig. S8).

Metal	hν (eV) for M-(OOH)/-$(O_2)^{2-}$	hν (eV) for M-$(O_2)^-$
Ti	2.95	3.25
Zr	4.61	4.94
Hf	4.66	5.04
Nb	3.48	3.99
Ta	4.56	4.21

S2.3 Time-Resolved *In Situ* UV-Vis Spectroscopy and Kinetic Parameter Optimization

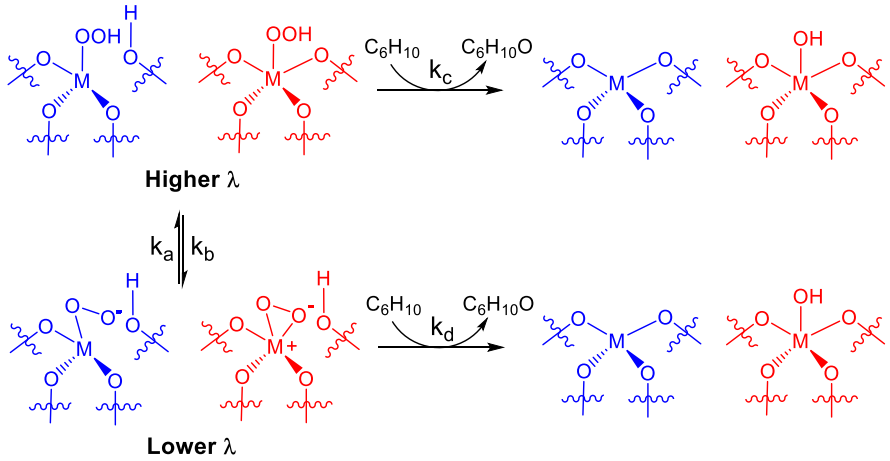

Scheme 1 (duplicated from main text). Interconversion and consumption of M-OOH/M-$(O_2)^{2-}$ (M-OOH) shown) and M-$(O_2)^{-}$ species upon reaction with C_6H_{10}. Color coding is for clarity: group IV (Ti, Zr, and Hf, blue) and V (Nb and Ta, red).

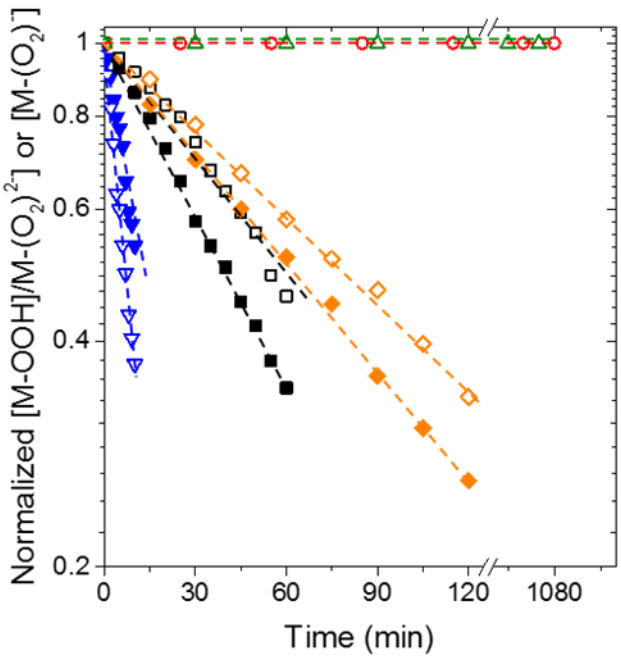

Figure 3 (duplicated from main text). Normalized surface coverages of M-OOH/M-$(O_2)^{2-}$ (open symbols) and M-$(O_2)^{-}$ (closed symbols) species as a function of time for $Ti_{1.0}$- (▼), $Zr_{1.0}$- (●), $Hf_{1.0}$- (▲), $Nb_{0.2}$- (■), and $Ta_{0.6}$-β (♦). Spectra were acquired *in situ* upon flowing C_6H_{10} in CH_3CN (0.1 M, 0.4 M H_2O, 1 cm^3 min^{-1}) over H_2O_2-activated samples (Section 2.4) at 313K. Closed symbols for $Zr_{1.0}$- and $Hf_{1.0}$-β coincide with the open symbols. Dashed lines are intended to guide the eye. $Nb_{0.2}$-β data is adapted from ref [6].

The change in surface coverage of the M-OOH/M-$(O_2)^{2-}$ and M-$(O_2)^-$ species depends on the summed rates of formation/consumption via interconversion and consumption by reaction with C_6H_{10}, which take the forms of:

$$\frac{d[M-(O_2)^-]}{dt} = k_a[M-OOH] - k_b[M-(O_2)^-] - k_d[M-(O_2)^-][C_6H_{10}] \quad \text{(S3)}$$

$$\frac{d[M-OOH]}{dt} = k_b[M-(O_2)^-] - k_a[M-OOH] - k_c[M-OOH][C_6H_{10}] \quad \text{(S4)}$$

where [M-OOH] and [M-$(O_2)^-$] represent the coverages (via UV-vis) of M-OOH/M-$(O_2)^{2-}$ and M-$(O_2)^-$, respectively, and k_x is the rate constant for step x in scheme 1. Pseudo first-order kinetics are assumed for the reaction between M-(O_2) intermediates and C_6H_{10}, as throughout the experiment the ratio of [C_6H_{10}] to number of metal atoms exceeds 10^5 in all cases. MATLAB™ is used to numerically estimate the kinetic parameters, by fitting the data (Fig. 3) to the coupled differential equations (eqns. S3 and S4). The initial guesses used for the rate constants were 0.01, 0.01, 0.001, 0.001 for k_a, k_b, k_c, and k_d, respectively. Changes of the initial values by an order of magnitude (increasing and decreasing) did not change the optimized parameter values.

Table S2. Numerically optimized rate constants, k_i (s^{-1}), for the interconversion of M-OOH/M-$(O_2)^{2-}$ and M-$(O_2)^-$ (Scheme 1) and reaction with C_6H_{10}.

Sample	k_a	k_b	k_c	k_d
$Ti_{1.0}$-β	$1.5\cdot10^{-3}$	$5.0\cdot10^{-4}$	$2.9\cdot10^{-2}$	$1.7\cdot10^{-4}$
$Nb_{0.6}$-β	$3.8\cdot10^{-6}$	$3.3\cdot10^{-4}$	$2.2\cdot10^{-7}$	$4.5\cdot10^{-3}$
$Ta_{0.6}$-β	$4.3\cdot10^{-3}$	$4.3\cdot10^{-3}$	$1.0\cdot10^{-4}$	$3.3\cdot10^{-3}$
$Zr_{1.0}$-β	-	-	$< 10^{-6}$	$< 10^{-6}$
$Hf_{1.0}$-β	-	-	$< 10^{-6}$	$< 10^{-6}$

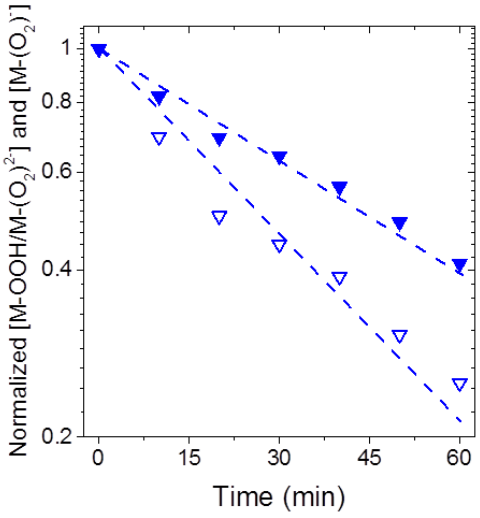

Figure S9. Change in the normalized surface coverage of M-OOH/M-$(O_2)^{2-}$ (open symbols) and M-$(O_2)^{-}$ (closed symbols) species as a function of time for $Ti_{1.0}$-BEA. Spectra were acquired *in situ* upon flowing *cis*-stilbene in CH_3CN (0.01 M *cis*-stilbene, 0.4 M H_2O, 0.25 cm^3 min^{-1}) over H_2O_2-activated samples (Section 2.4) at 313K. To avoid misinterpretation, it should be noted that the Y-axis is log scale.

S3.0 Additional Kinetic Data, Derivation of Relevant Rate Expressions and Transition-State Theory

S3.1 Derivation of Full Rate Expression for C_6H_{10} Epoxidation

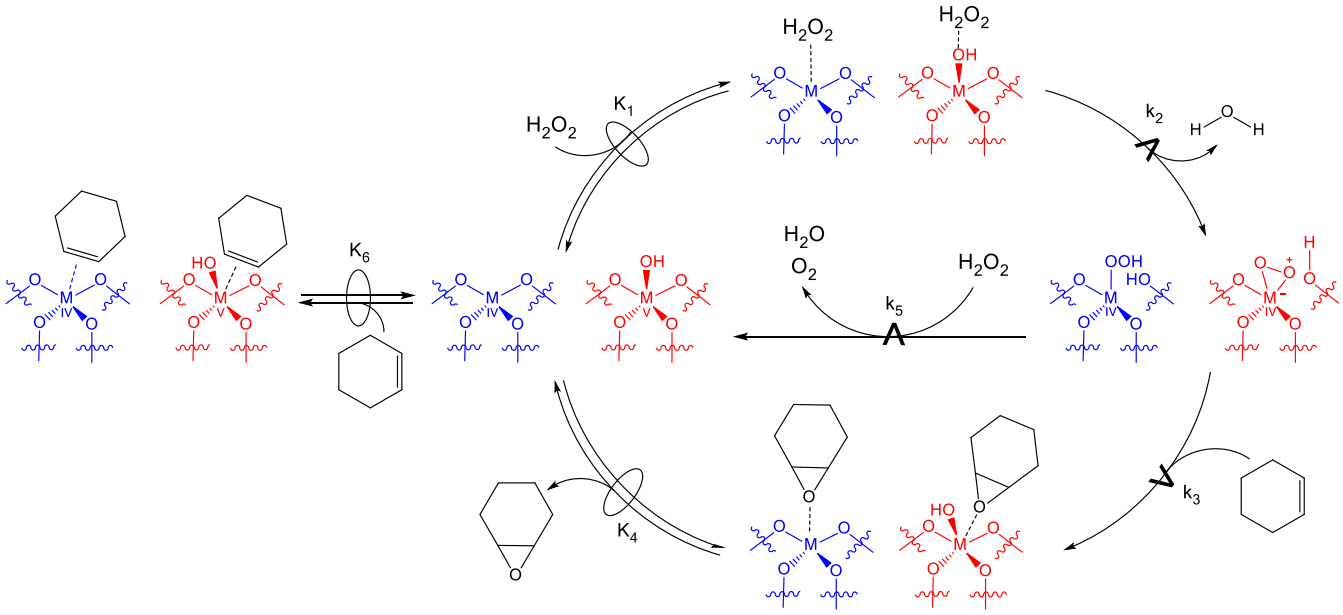

Scheme 2 (copied from main text). Proposed mechanism for the epoxidation of C_6H_{10} with H_2O_2 over group IV (Ti, Zr, and Hf, M-OOH shown, blue) and group V (Nb and Ta, red) M-β. The symbol ⇄ represents a quasi-equilibrated step, while → represents a kinetically relevant step. Note, the unoccupied metal atoms are meant to be representations of an empty site, rather than suggest all metal atoms exist as closed sites, as both open and closed sites likely exist in these materials (see characterization results, Section 2.2).

Scheme 2 shows a series of elementary steps that account for the measured effects of $[C_6H_{10}]$ and $[H_2O_2]$ (Fig. 4) on both rates of C_6H_{10} epoxidation.[6] The catalytic cycle involves the quasi-equilibrated adsorption of H_2O_2 (step 1),[5-7] followed by the irreversible activation of H_2O_2 (step 2) to form a pool of M-$(O_2)^-$ (group V, superoxide)[6] and M-OOH/M-$(O_2)^{2-}$ (group IV, hydroperoxide/peroxide)[8-11] active intermediates (referred to collectively as M-(O_2)), which then react with C_6H_{10} to form $C_6H_{10}O$ (step 3), followed by $C_6H_{10}O$ desorption (step 4) or decompose by reaction with H_2O_2 (step 5). Measured C_6H_{10} epoxidation rates represent the kinetically relevant reaction of the active form of the oxidizing surface intermediate with a C_6H_{10} molecule:

$$r_E = k_3[M-O_2][C_6H_{10}] \tag{S5}$$

where r_E is the rate of C_6H_{10} epoxidation, $[M-(O_2)]$ is the collective coverage of M-OOH/M-$(O_2)^{2-}$ (group IV) and M-$(O_2)^-$ (group V), k_x is the rate constant for step x in Scheme 2, and $[C_6H_{10}]$ is the concentration of C_6H_{10}. Application of the pseudo-steady state hypothesis to the M-(O_2) intermediates, results in:

$$r_E = \frac{k_2 k_3 K_1 [C_6H_{10}][H_2O_2][*]}{(k_3[C_6H_{10}] + k_5[H_2O_2])} \quad \text{(S6)}$$

Where K_x is the equilibrium constant for step x and [*] is the total number of empty (i.e., unoccupied) M atoms. An expression for [*] is given by the summation of all likely surface-bound intermediates:

$$[L] = [*] + [C_6H_{10}*] + [H_2O_2*] + [M-(O_2)] + [C_6H_{10}O*] \quad \text{(S7)}$$

where [L] is the total number of M atoms, [M-(O_2)] is the pool of M-OOH/M-$(O_2)^{2-}$ and M-$(O_2)^-$ intermediates, and [C_6H_{10}*], [H_2O_2*], and [$C_6H_{10}O$*] are surface-bound C_6H_{10}, H_2O_2, and $C_6H_{10}O$ molecules, respectively. Equation S7 can then be restated in terms of the rate and equilibrium constants, as well as liquid-phase reactant concentrations and unoccupied M atoms by application of the PSSH to each specie to yield:

$$[L] = [*] + K_6[C_6H_{10}][*] + K_1[H_2O_2][*] + \frac{k_2 K_1 [H_2O_2][*]}{(k_3[C_6H_{10}] + k_5[H_2O_2])} + K_4[C_6H_{10}O][*] \quad \text{(S8)}$$

Substitution of equation S8 into S6 yields the full rate expression for $C_6H_{10}O$ formation:

$$\frac{r_E}{[L]} = \frac{\frac{k_2 k_3 K_1 [C_6H_{10}][H_2O_2]}{(k_3[C_6H_{10}] + k_5[H_2O_2])}}{1 + K_6[C_6H_{10}] + K_1[H_2O_2] + \frac{k_2 K_1 [H_2O_2]}{(k_3[C_6H_{10}] + k_5[H_2O_2])} + K_4[C_6H_{10}O]} \quad \text{(S9)}$$

which is consistent with equation 2 from the main text.

S3.2 Derivation of Full Rate Expression for H_2O_2 Decomposition

Scheme 2 shows a series of elementary steps that account for the measured effects of $[C_6H_{10}]$ and $[H_2O_2]$ (Fig. 4) on both rates of H_2O_2 decomposition.[6] The catalytic cycle involves the quasi-equilibrated adsorption of H_2O_2 (step 1),[5-7] followed by the irreversible activation of H_2O_2 (step 2) to form a pool of M-$(O_2)^-$ (group V, superoxide)[6] and M-OOH/M-$(O_2)^{2-}$ (group IV, hydroperoxide/peroxide)[8-11] active intermediates (referred to collectively as M-(O_2)), which then or decompose by reaction with H_2O_2 (step 5). Measured C_6H_{10} epoxidation rates represent the kinetically relevant reaction of the active form of the oxidizing surface intermediate with a C_6H_{10} molecule:

$$r_D = k_5[M-O_2][H_2O_2] \tag{S10}$$

where r_D is the rate of C_6H_{10} epoxidation, [M-(O_2)] is the collective coverage of M-OOH/M-$(O_2)^{2-}$ (group IV) and M-$(O_2)^-$ (group V), k_x is the rate constant for step x in Scheme 2, and $[H_2O_2]$ is the concentration of H_2O_2. Application of the pseudo-steady state hypothesis to the M-(O_2) intermediates, results in:

$$r_D = \frac{k_2 k_5 K_1 [H_2O_2]^2 [*]}{(k_3[C_6H_{10}] + k_5[H_2O_2])} \tag{S11}$$

Where K_x is the equilibrium constant for step x and [*] is the total number of empty (i.e., unoccupied) M atoms. An expression for [*] is given by the summation of all likely surface-bound intermediates:

$$[L] = [*] + [C_6H_{10}*] + [H_2O_2*] + [M-(O_2)] + [C_6H_{10}O*] \tag{S12}$$

where [L] is the total number of M atoms, [M-(O_2)] is the pool of M-OOH/M-$(O_2)^{2-}$ and M-$(O_2)^-$ intermediates, and $[C_6H_{10}*]$, $[H_2O_2*]$, and $[C_6H_{10}O*]$ are surface-bound C_6H_{10}, H_2O_2, and $C_6H_{10}O$ molecules, respectively. Equation S12 can then be restated in terms of the rate and equilibrium constants, as well as liquid-phase reactant concentrations and unoccupied M atoms by application of the PSSH to each specie to yield:

$$[L] = [*] + K_6[C_6H_{10}][*] + K_1[H_2O_2][*] + \frac{k_2 K_1 [H_2O_2][*]}{(k_3[C_6H_{10}] + k_5[H_2O_2])} + K_4[C_6H_{10}O][*] \tag{S13}$$

Substitution of equation S13 into S10 yields the full rate expression for H_2O_2 decomposition:

$$\frac{r_D}{[L]} = \frac{\dfrac{k_2 k_5 K_1 [H_2O_2]^2}{(k_3[C_6H_{10}] + k_5[H_2O_2])}}{1 + K_6[C_6H_{10}] + K_1[H_2O_2] + \dfrac{k_2 K_1 [H_2O_2]}{(k_3[C_6H_{10}] + k_5[H_2O_2])} + K_4[C_6H_{10}O]} \quad \text{(S14)}$$

At high $[H_2O_2]$:$[C_6H_{10}]$ reactant ratios, M-(O_2) species are the most abundant surface intermediates (MASI) on all M-β (Section 2.2, Fig. 3 in the main text), which simplifies equation S14 to yield:

$$\frac{r_D}{[L]} = k_5[H_2O_2] \quad \text{(S15)}$$

Figure S11 shows H_2O_2 decomposition rates for Ti-, Nb-, and Ta-β as a function of $[H_2O_2]$ at constant $[C_6H_{10}]$ under a M-(O_2) MASI. In all cases, H_2O_2 decomposition rates depend linearly on $[H_2O_2]$, which is in excellent agreement with equation S14. Collectively, these data, in comparison to the derived rate expressions, strongly suggest that H_2O_2 decomposition occurs via a bimolecular reaction pathway, where H_2O_2 reacts directly with the M-(O_2) intermediates.

Total rates of H_2O_2 consumption (r_{H2O2}) are given by the sum of equations S9 and S14 to yield:

$$\frac{r_{H2O2}}{[L]} = \frac{\dfrac{k_2 k_5 K_1 [H_2O_2]^2}{(k_3[C_6H_{10}] + k_5[H_2O_2])} + \dfrac{k_2 k_3 K_1 [C_6H_{10}][H_2O_2]}{(k_3[C_6H_{10}] + k_5[H_2O_2])}}{1 + K_6[C_6H_{10}] + K_1[H_2O_2] + \dfrac{k_2 K_1 [H_2O_2]}{(k_3[C_6H_{10}] + k_5[H_2O_2])} + K_4[C_6H_{10}O]} \quad \text{(S16)}$$

The selectivity for H_2O_2 use in epoxidations can then be cast as the ratio of r_{H2O2} to r_E (α, i.e., equation S16 over S9) to result in:

$$\alpha = 1 + \frac{k_5[H_2O_2]}{k_3[C_6H_{10}]} \quad \text{(S17)}$$

where the numerator (i.e., $k_5[H_2O_2]$) and denominator (i.e., $k_3[C_6H_{10}]$) may be estimated for Ti-, Nb-, and Ta-β by inspection of Figs. 3 and S11. Table S3 shows the ratio of $k_5[H_2O_2]$:$k_3[C_6H_{10}]$ for Ti-, Nb-, and Ta-β under conditions that result in a $C_6H_{10}O$ MASI (i.e., the conditions in Fig. 3b). The relative values of $k_5[H_2O_2]$:$k_3[C_6H_{10}]$ for Ti-, Nb-, and Ta-β under a $C_6H_{10}O$ MASI shows that $k_3[C_6H_{10}] >> k_5[H_2O_2]$.

Table S3. Calculated ratios of $k_5[H_2O_2]:k_3[C_6H_{10}]$ using interpolated values from Figs. 3 and S11 for $Nb_{0.6}$-, $Ta_{0.6}$-, and $Ti_{1.0}$-β at conditions that result in a $C_6H_{10}O$ MASI (i.e., conditions in Fig. 3b).

Sample	$k_5[H_2O_2]/k_3[C_6H_{10}]$
$Nb_{0.6}$-β	0.05
$Ta_{0.6}$- β	0.0009
$Ti_{1.0}$- β	0.025

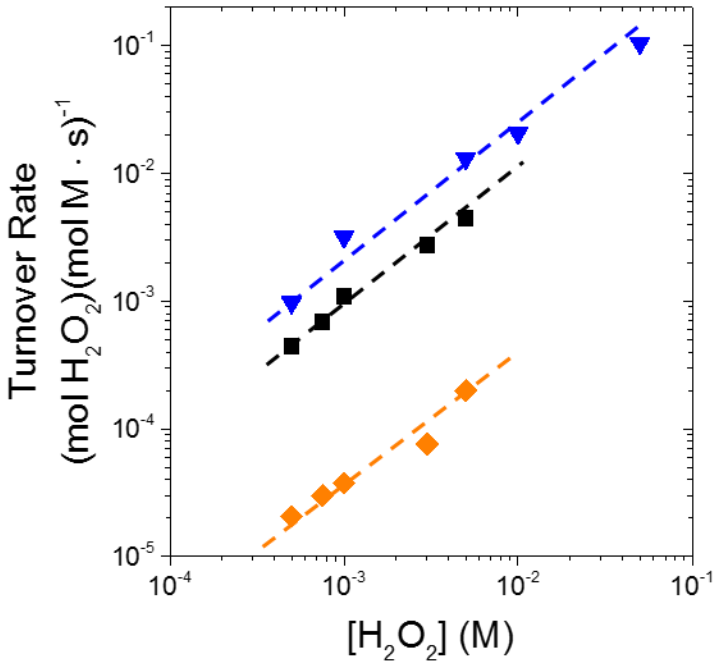

Figure S10. H_2O_2 decomposition rates as a function of [H_2O_2] over $Nb_{0.6}$-β (■, 0.05 M C_6H_{10}, 313 K), $Ta_{0.6}$-β (♦, 2 mM C_6H_{10}, 313 K), and $Ti_{1.0}$-β (▼, 0.01 M C_6H_{10}, 313 K). Dashed lines are intended to guide the eye. $Nb_{0.6}$-β data is adapted from ref [6].

S3.3 Transition-State Theory for Measurement of Activation Enthalpies and Entropies

Transition-state theory (TST) is used to relate the stability of the reference state (e.g., M-(O_2) intermediate) to an activated complex that leads to reaction (i.e., the transition state).[6,12,13] TST, when combined with our proposed mechanism (Scheme 2), proposes that the reactant species (i.e., M-(O_2), H_2O_2, and C_6H_{10}) exist in equilibrium with the transition state to yield:

$$\frac{r_E}{[L]} = \frac{k_B T}{h} K_E^{\ddagger}[C_6H_{10}] \tag{S15}$$

$$\frac{r_E}{[L]} = \frac{k_B T}{h} K_D^{\ddagger}[H_2O_2] \tag{S16}$$

where k_B is Boltzmann's constant, h is Planck's constant, T is the temperature in kelvin, $K_E^{\ddagger}$ and $K_D^{\ddagger}$ are the Transition-state equilibrium constants for epoxidation and H_2O_2 decomposition, respectively, and [C_6H_{10}] is the concentration of C_6H_{10}. Values of $K_E^{\ddagger}$ and $K_D^{\ddagger}$ may be expressed in terms of free energy, via the Eyring equation, to result in:

$$K_x^{\ddagger} = e^{-\Delta G_x^{\ddagger}/RT} = e^{-\Delta H_x^{\ddagger}/RT} e^{\Delta S_x^{\ddagger}/R} \tag{S17}$$

Where R is the ideal gas constant and $\Delta G^{\ddagger}$, $\Delta H^{\ddagger}$, and $\Delta S^{\ddagger}$ is the Gibb's free energy, enthalpy, and entropy of activation, respectively. Figure S8 shows measured values for $K_E^{\ddagger}$ and $K_D^{\ddagger}$ as a function of inverse temperature for all M-β.

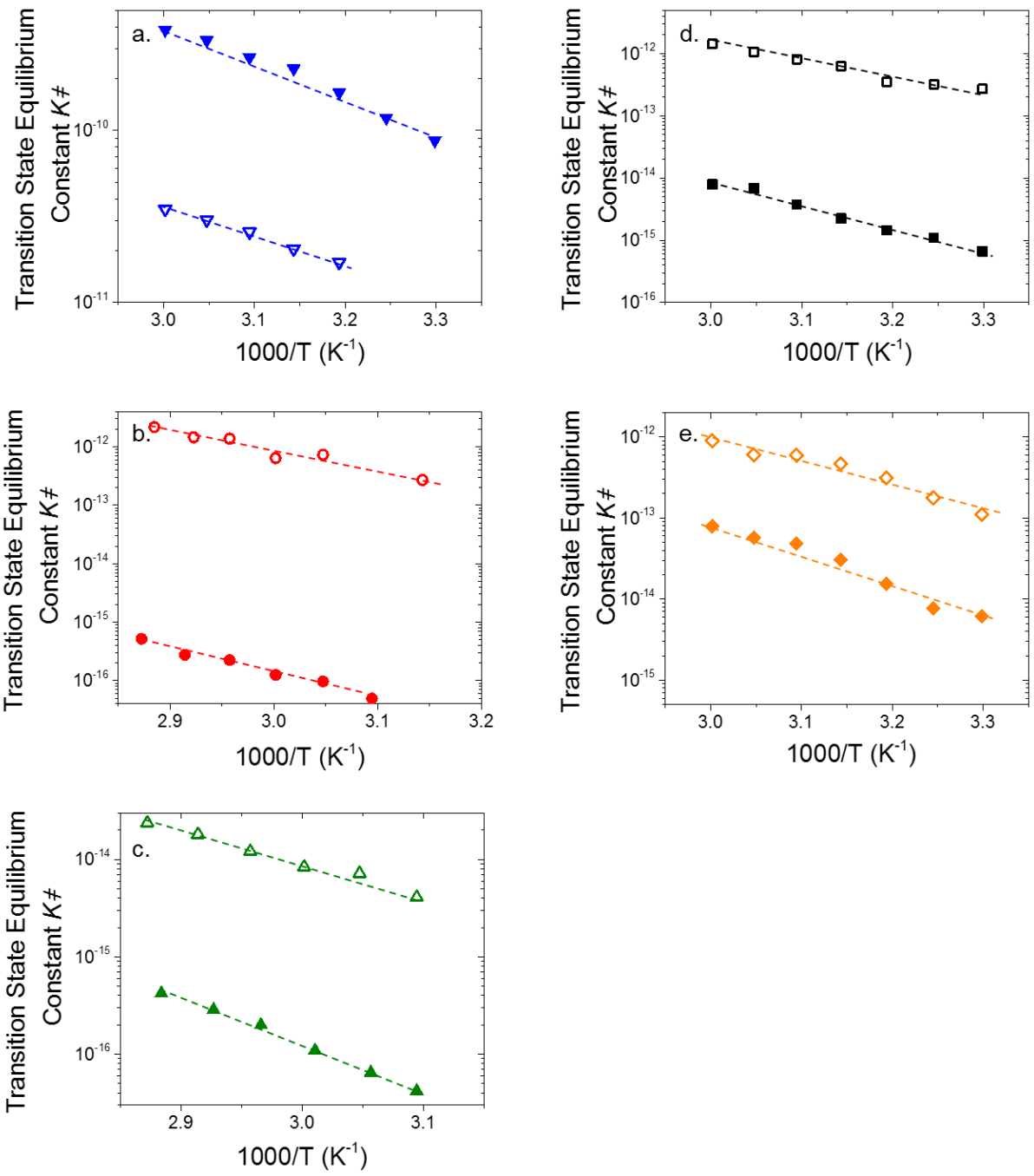

Figure S11. Transition state equilibrium constants for C_6H_{10} epoxidation ($K_E^{\ddagger}$, closed symbols) and H_2O_2 decomposition ($K_D^{\ddagger}$, open symbols) as functions of inverse temperature on (a) $Ti_{1.0}$-β (▼, 0.5 mM C_6H_{10}, 0.05 M H_2O_2), (b) $Zr_{1.0}$-β (●, 0.5 mM C_6H_{10}, 0.1 M H_2O_2), (c) $Hf_{1.0}$-β (▲, 0.5 mM C_6H_{10}, 0.1 M H_2O_2), (d) $Nb_{0.6}$-β (■, 0.05 M C_6H_{10}, 1 mM H_2O_2), and (d) $Ta_{0.6}$-β (♦, 0.01 M C_6H_{10}, 1 mM H_2O_2) under a M-(O_2) MASI. Error bars were omitted for clarity. In all reported data, error was < 7%. Lines represent fits to the Eyring equation (equation S5). $Nb_{0.6}$-β data is adapted from ref [6].

S4. Effects of Metal Electronegativity (Pauling and Mulliken) on Activation Enthalpies and Measured CD_3CN Adsorption Enthalpies

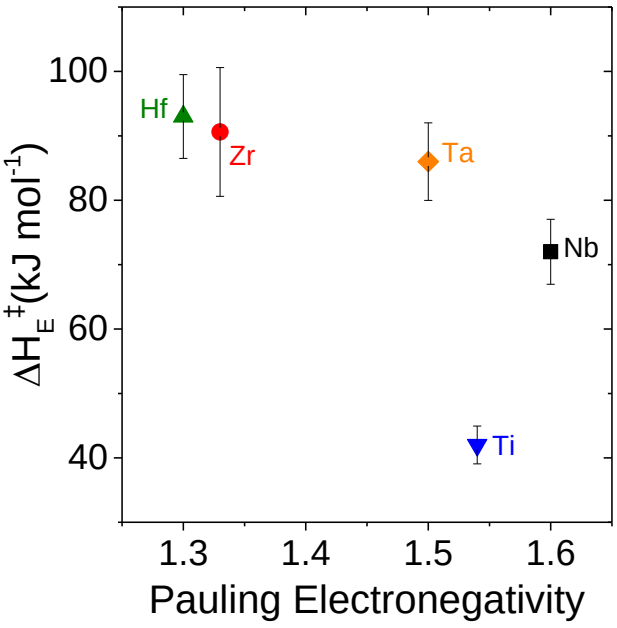

Figure S12. Activation enthalpies for C_6H_{10} epxoidation ($\Delta H_E^{\ddagger}$), measured on a M-(O_2) MASI (Fig. S8), as a function of metal-atom Pauling electronegativity on $Ti_{1.0}$-β (▼), $Zr_{1.0}$-β (●), $Hf_{1.0}$-β (▲), $Nb_{0.6}$-β (■), and $Ta_{0.6}$-β (♦).

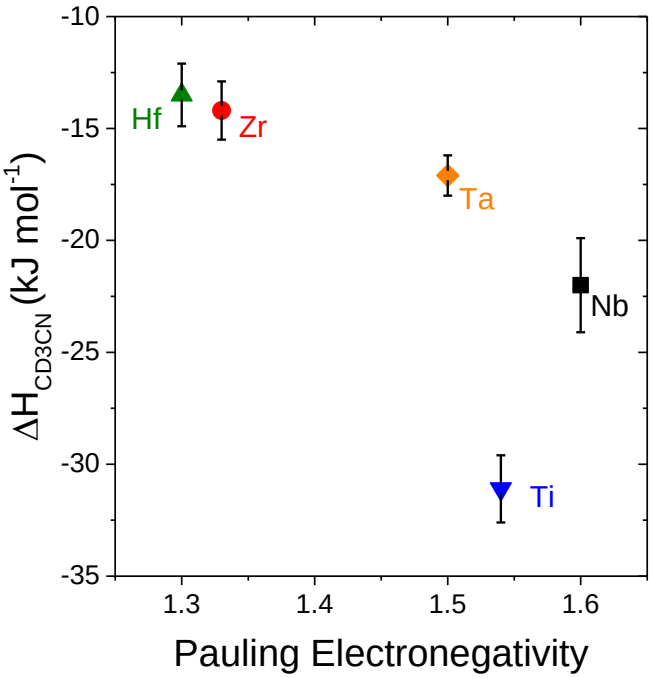

Figure S13. Measured CD_3CN adsorption enthalpies (Section 2.2) as a function of metal-atom Pauling electronegativity on $Ti_{1.0}$-β (▼), $Zr_{1.0}$-β (●), $Hf_{1.0}$-β (▲), $Nb_{0.6}$-β (■), and $Ta_{0.6}$-β (♦).

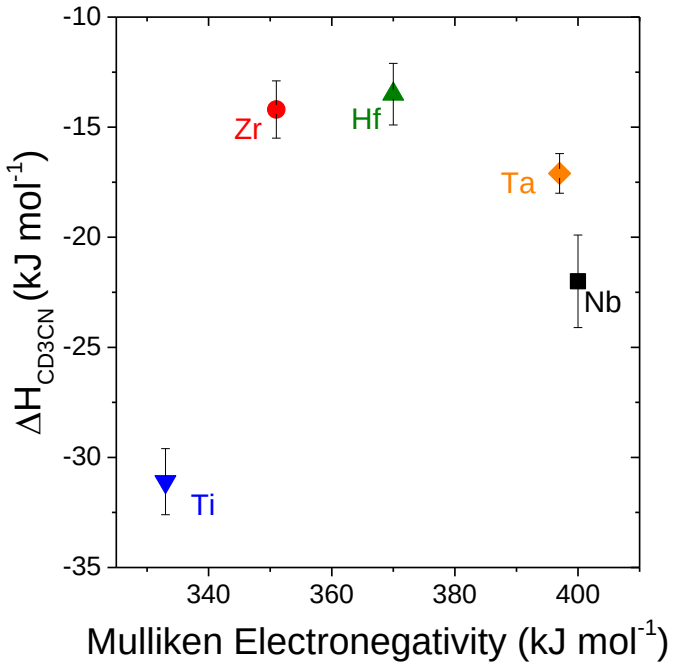

Figure S14. Measured CD_3CN adsorption enthalpies (Section 2.2) as a function of metal-atom Mulliken electronegativity on $Ti_{1.0}$-β (▼), $Zr_{1.0}$-β (●), $Hf_{1.0}$-β (▲), $Nb_{0.6}$-β (■), and $Ta_{0.6}$-β (♦). Mulliken electronegativity values are adapted from ref [14].

References:

(1) Boronat, M.; Concepción, P.; Corma, A.; Renz, M.; Valencia, S. *J. Catal.* **2005**, *234*, 111-118.
(2) Roy, S.; Bakhmutsky, K.; Mahmoud, E.; Lobo, R. F.; Gorte, R. J. *ACS Catal.* **2013**, *3*, 573-580.
(3) Sushkevich, V. L.; Vimont, A.; Travert, A.; Ivanova, I. I. *J. Phys. Chem. C* **2015**, *119*, 17633-17639.
(4) Harris, J. W.; Cordon, M. J.; Di Iorio, J. R.; Vega-Vila, J. C.; Ribeiro, F. H.; Gounder, R. *J. Catal.* **2016**, *335*, 141-154.
(5) Madon, R. J.; Boudart, M. *Ind. Eng. Chem. Fundam.* **1982**, *21*, 438-447.
(6) Bregante, D. T.; Priyadarshini, P.; Flaherty, D. W. *J. Catal.* **2017**, *348*, 75-89.
(7) Ruddy, D. A.; Tilley, T. D. *J. Am. Chem. Soc.* **2008**, *130*, 11088-11096.
(8) Wilson, N. M.; Bregante, D. T.; Priyadarshini, P.; Flaherty, D. W. *Catalysis* **2017**, *29*, 122-212.
(9) Lin, W.; Frei, H. *J. Am. Chem. Soc.* **2002**, *124*, 9292.-9298
(10) Bonino, F.; Damin, A.; Ricchiardi, G.; Ricci, M.; Spano, G.; D'Aloisio, R.; Zecchina, A.; Lamberti, C.; Prestipino, C.; Bordiga, S. *J. Phys. Chem. B* **2008**, *108*, 3573-3583.
(11) Bordiga, S.; Damin, A.; Bonino, F.; Ricchiardi, G.; Lamberti, C.; Zecchina, A. *Angew. Chem. Int. Ed. Engl.* **2002**, *41*, 4734-4737.
(12) Flaherty, D. W.; Iglesia, E. *J. Am. Chem. Soc.* **2013**, *135*, 18586-18599.
(13) Wilson, N. M.; Flaherty, D. W. *J. Am. Chem. Soc.* **2016**, *138*, 574-586.
(14) Gunther, W. R.; Michaelis, V. K.; Griffin, R. G.; Román-Leshkov, Y. *J. Phys. Chem. C* **2016**, *120*, 28533-28544.